

Design, Modeling, and Experiment of a Novel Wire-driven Robotic Fish

Runtong Ai^{1,2,3,4†}, Bingxiong Wang^{1,2,3,4†}, Guohua Yu^{1,2,3,4†},
Yang Liu^{1,2,3,4†}, Wenbo Li^{1,2,3,4†}, Yan Meng^{1,2,3,4†}, Jincun Liu^{1,2,3,4*}

¹*National Innovation Center for Digital Fishery, China Agricultural University, Beijing 100083, China.

²Key Laboratory of Smart Farming Technologies for Aquatic Animals and Livestoc, Ministry of Agriculture and Rural Affairs, China Agricultural University, Beijing 100083, China.

³Beijing Engineering and Technology Research Centre for Internet of Things in Agriculture, China Agricultural University, Beijing 100083, China.

⁴College of Information and Electrical Engineering, China Agricultural University, Beijing 100083, China.

*Corresponding author(s). E-mail(s): liujincun@cau.edu.cn;

†These authors contributed equally to this work.

Abstract

In this paper, a novel wire-driven robotic fish is proposed and developed. The innovation lies in achieving reciprocating tail fin oscillation through continuous motor rotation, with adjustable oscillation amplitude. The robotic fish is capable of swimming without frequent motor reversals and can dynamically adjust its tail fin oscillation amplitude and frequency to adapt to different environmental demands. First, the paper presents a detailed description of the robotic fish's mechatronic design and working principle. Second, a comprehensive kinematic analysis is conducted. The dynamic model of the robotic fish is established using the Newton-Euler method, and the hydrodynamic parameters in the model are optimally identified through a data-driven parameter identification approach. To validate the performance of the robotic fish and the accuracy of the dynamic model, relevant experiments and simulations are conducted, and their results are compared. The simulation results demonstrate that the robotic fish exhibits excellent swimming performance and reveal the effectiveness of the dynamic model. Finally, field experiments are conducted, demonstrating the robotic fish's good

swimming stability and environmental adaptability. The research in this paper provides insights for enhancing the practical value of robotic fish in real-world applications.

Keywords: Robotic fish, wire-driven mode, dynamic modeling, field experiments

1 Introduction

With the development and utilization of marine resources, the Unmanned Underwater Vehicles (UUVs), including Remotely Operated Underwater Vehicles (ROVs) and Autonomous Underwater Vehicles (AUVs), have become new tools for human exploration of the ocean. Inspired by the swimming mechanisms of biological fish, robotic fish have emerged over the past three decades as a new type of AUV[1]. These robotic fish exhibit exceptional maneuverability, stealth, and biological friendliness[2]. In 1994, the Massachusetts Institute of Technology (MIT) introduced the world's first robotic fish, RoboTuna[3]. Since then, research related to the structural design[4], motion control[5], and other areas has flourished, with widespread applications in underwater exploration[6, 7], environmental monitoring[8], aquaculture[9], and more. The mechatronic design of robotic fish can generally be classified into two categories based on their main structural design: rigid robotic fish and soft robotic fish. Rigid robotic fish typically consist of a rigid head, with either a single-joint oscillating rigid tail[10, 11] or a multi-joint tail[12]. Although rigid robotic fish can replicate the swimming characteristics of fish, they suffer from significant friction between adjacent links, an imbalanced load distribution, and unstable power output from the servo motors. Soft robotic fish possess excellent deformability, flexibility, and adaptability. They can exhibit continuous body undulatory motions that rigid robotic fish cannot achieve, helping to reduce power consumption and improve swimming efficiency[13, 14]. However, soft robotic fish systems involve complex fluid dynamics, making it difficult to directly establish accurate models. Additionally, long-term operation in complex aquatic environments can lead to issues such as material aging and wear. Moreover, their structural design limits their load-bearing capacity[1].

Biological research indicates that in fish species that rely on their tail fins for primary propulsion, the muscles at the front of the body perform most of the propulsion work, while the muscles at the rear of the body are primarily responsible for transmitting force to the tail and tail fin to generate oscillation[15]. Based on this biological principle, researchers have proposed a wire-driven robotic fish model[16–18]. The wire-driven robotic fish uses lines on both sides of the tail to drive a fish-like spine, enabling tail oscillation that closely mimics the movement mechanism of real fish. Compared to multi-joint robotic fish, the number of actuators in a wire-driven robotic fish can be significantly reduced, requiring as few as one servo motor. Additionally, its tail exhibits greater continuity than that of multi-joint robotic fish. Compared to fully soft materials, wire-driven robotic fish offer stable mechanical properties, making them more suitable for further development. Estarki et al. proposed a robotic fish that combines a wire-driven mechanism with a flexible structure. This device is capable of achieving

stable and reliable lateral oscillation behaviors under both low-frequency and high-frequency driving conditions, demonstrating excellent motion adaptability and system robustness[19]. Chen et al. designed a fish-like autonomous cruising robot driven by a wire mechanism. The robotic fish uses a flexible tail fin, driven by a wire structure, as the primary propulsor, with the movement of the tail fin directly controlled by a servo motor and wires[20]. Liang et al. designed a wire-driven flexible tail fin vector propulsion system, where the fish tail can oscillate in all directions[21]. Liao et al. proposed a wire-driven elastic robotic fish, which uses multiple wires to simulate fish muscles and incorporates a fish-shaped spine design based on elastic components to achieve compliant simulation of fish swimming gaits[17]. Qiu et al. designed and implemented a fully functional tendon-driven robotic fish with a variable stiffness passive tail fin. This system utilizes a unique tendon-driven structure with a torsional spring, motor, and spring to achieve the variable stiffness passive tail fin[22]. Wang et al. designed and implemented a dual-tendon-driven robotic dolphin tail with passive joints. Under the influence of the dual-tendon driving mechanism, the robotic dolphin tail can achieve omnidirectional motion, ensuring high maneuverability[23]. Zhong et al. developed a robotic fish with an active wire-driven body and a flexible tail, achieving a maximum speed of 2.15 BL/s and a turning rate of 63°/s[24]. Liu et al. proposed and developed a new type of continuum robotic dolphin, "ConRoDolI," which uses a dual-tendon-driven continuum mechanism to replicate the twisting and bending motions of the dolphin's caudal and thoracic vertebrae[25]. Jiang et al. developed a cable-driven tensegrity-based robotic tuna, in which a tendon cable passes through seven serially connected V-shaped tensegrity joints to form a compliant and controllable tail-wave propagation chain[26]. These wire-driven robotic fish can easily achieve more complex functions and replicate fish swimming behaviors more realistically, without the need for redundant actuators. However, these wire-driven robotic fish rely on the reciprocating motion of motors/servos to drive the tail's oscillation. This driving method requires frequent switching of the motor's rotation direction, leading to periodic acceleration and deceleration processes, which can cause motor overheating and an increased failure rate. Moreover, this type of driving mechanism has limitations in terms of motion performance, often struggling to achieve high swimming frequencies, which significantly restricts further improvement in the performance of the robotic fish. Therefore, it is essential to explore a wire-driven robotic fish that uses continuous motor rotation to achieve tail fin oscillation.

In the design of a robotic fish driven by continuous motor rotation, the motor does not need to frequently reverse its direction, allowing the robotic fish to achieve higher oscillation frequencies while also saving energy consumption. Clapham R. J. et al. designed the robotic fish "iSplashI," which uses external power supply and a continuously rotating motor to achieve a tail beat frequency of up to 6.6 Hz, with a maximum swimming speed of approximately 2.8 BL/s[27]. White C. H. designed the robotic fish "TunabotFlex," which achieved a maximum swimming speed of 4.6 BL/s at a driving frequency of 8 Hz[28]. Yu et al. developed a small, tethered high-speed robotic fish driven by a single motor, combining a motor and a passive linkage mechanism. This design achieved a maximum swimming speed of 3.07 BL/s and excellent turning maneuverability[29]. van den Berg S. C. et al. developed a high-speed robotic

fish driven by a single motor, where the reciprocating motion of the drive wire is achieved through a gear-shifting mechanism driven by the continuous rotation of the motor. This design achieved a maximum swimming speed of 2.02 BL/s at a driving frequency of 5.46 Hz[30]. However, while the propulsion scheme, where the motor continuously rotates to drive the tail oscillation, allows the robotic fish to achieve excellent swimming performance, the amplitude of the tail's oscillation remains difficult to adjust. A fixed oscillation amplitude can only respond to a single environment, resulting in limited flexibility and potential hydrodynamic efficiency losses at certain frequencies. A variable oscillation amplitude is more adaptable, allowing for adjustment of the amplitude at different frequencies, which helps the system achieve better propulsion efficiency and hydrodynamic performance, enhancing environmental adaptability. Therefore, it is worthwhile to explore the possibility of achieving adjustable tail fin oscillation amplitude while utilizing continuous motor rotation to drive the tail's oscillation.

To address the aforementioned problems effectively, in this paper, a novel wire-driven robotic fish is proposed, which achieves continuous motor rotation to drive tail fin oscillation, variable tail fin oscillation amplitude, and the ability to adjust the tail fin oscillation frequency by changing the motor speed. The main contributions of this paper can be summarized in the following three aspects:

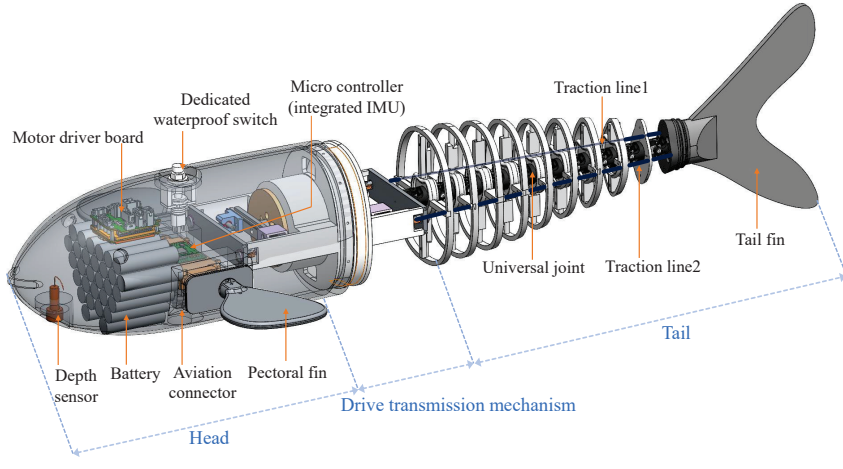
- A novel wire-driven robotic fish is designed and implemented, where the tail fin oscillation is driven by continuous motor rotation, and the oscillation amplitude can be adjusted by switching the motor's rotation direction.
- Kinematic and dynamic models of the robotic fish are established. Model parameters are identified using a data-driven approach, bringing the models closer to actual motion patterns.
- Extensive simulations and real swimming experiments are conducted to validate the feasibility of the mechanism design and models. Field experiments are carried out to verify the robot fish's maneuverability and practical application potential.

The remainder of this paper is organized as follows: Section 2 introduces the overall mechatronic design and working principles of the novel wire-driven robotic fish. Section 3 presents the kinematic and dynamic models of the robotic fish. Section 4 provides the simulation and experimental results. Section 5 demonstrates the field experiments to verify the practical application potential of the robotic fish.

2 Mechatronic Design of the Robotic Fish

2.1 Overview of the Robotic Fish

A novel wire-driven robotic fish is proposed in this paper, as shown in Figure 1. The robotic fish achieves reciprocating tail fin motion through continuous motor rotation, with adjustable tail fin oscillation amplitude and frequency. The robotic fish consists of three main parts: 1) the head compartment; 2) the drive transmission mechanism, as shown in Figure 2; 3) the tail joint compartment. Table 1 lists the basic design parameters of the robotic fish.



(a)



(b)

Fig. 1: Overview of robotic fish. (a) Conceptual design. (b) Robotic fish swimming in the river.

The head compartment shell is fabricated from nylon material, offering excellent properties of wear resistance, heat resistance, and impact resistance. Internally, it houses the power system, pectoral fin actuation system, dedicated waterproof switch, aviation connector, micro controller (integrated IMU), motor driver board, and depth sensor. The power system consists of parallel-connected lithium battery packs evenly distributed at the bottom of the head compartment, providing stable energy supply for the robotic fish. The pectoral fin actuation system is composed of symmetrically arranged servo motors, which are connected to the external pectoral fins through rotary shafts sealed with compression seals, generating yaw and pitch torques for the robotic fish. The upper part of the head compartment features a dedicated waterproof switch with a self-locking function, used to control the main power of the robotic fish. The lower part of the head compartment is equipped with an aviation connector and a

Table 1: Basic design parameters of the robotic fish.

Items	Characteristics
Length × width × height	950mm(L) × 410mm(W) × 170mm(H)
Weight	8.25kg
Power supply	24V DC
Brushless motor	HaoJi8110
Controller	STM32F407
Servo motor	HS-7980
IMU	JY901B
Depth sensor	MS5837
Communication module	E62-433T30D

depth sensor. The aviation connector is used for charging the lithium batteries, while the depth sensor monitors depth variations.

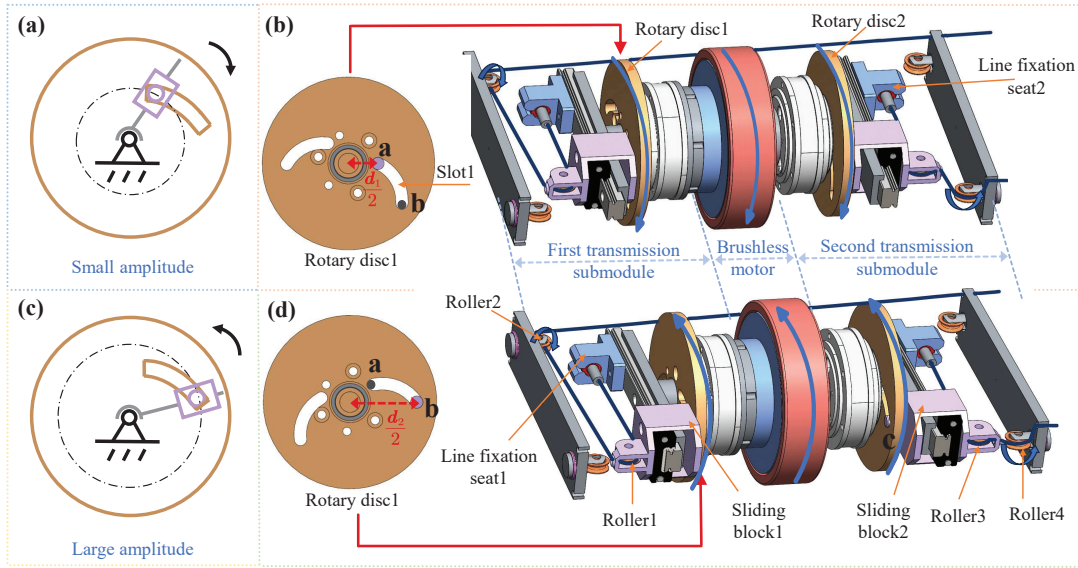


Fig. 2: Drive transmission module design. (a) Small-amplitude mechanical schematic. (b) Motor rotating forward. (c) Large-amplitude mechanical schematic. (d) Motor rotating in reverse.

As illustrated in Figure 2, the drive transmission module consists of three parts: the motor, the first transmission submodule, and the second transmission submodule. Centered on the motor, the first and second transmission submodules are symmetrically distributed on either side. The first transmission submodule is connected to the tail fin via Traction Line 1, while the second transmission submodule is connected

via Traction Line 2. The motor's rotation direction directly influences the oscillation amplitude of the tail fin. When the motor rotates continuously in the forward direction, the first and second transmission submodules drive the tail fin to oscillate with a small amplitude; when the motor rotates continuously in the reverse direction, the tail fin oscillates with a large amplitude. Meanwhile, changes in motor speed are transmitted to the tail fin through the two transmission submodules, thereby adjusting the tail fin oscillation frequency. The oscillation frequency of the tail fin is proportional to the motor's rotational frequency. The housing of the drive transmission module is fabricated from aluminum alloy and embedded within the head compartment shell.

The tail joint compartment consists of ten joints, each adopting an elliptical base profile with gradually decreasing cross-sectional areas to maintain a streamlined tail shape. The tail joints are fixed by adjacent pairs of universal joints. Universal joints made of stainless steel are strung along a nickel-titanium alloy wire to form a spine, which enhances the tail's elastic recovery. The traction lines are made of nylon. The tail fin, fabricated from nylon material, is designed to remain undeformed during motion. A skin covers the tail joint compartment and connects to the drive transmission module, creating a sealed and waterproof environment.

2.2 Working Principle

The motor, serving as the driving unit, acts as the power source for the robotic fish's swimming. A rotary disc is employed to adjust the oscillation amplitude of the tail fin. As shown in Figure 2, slots are designed on the rotary disc, allowing the sliding blocks to latch at either end of the slots to regulate the oscillation amplitude. The layout of the second transmission submodule is similar to that of the first. Sliding block 1 moves within slot 1 on rotary disc 1, while sliding block 2 moves within slot 2 on rotary disc 2.

The motor's rotation direction affects the circular motion's diameter d , resulting in tail oscillations with different amplitudes. This mechanism provides two discrete amplitude options: a larger amplitude and a smaller amplitude. As shown in Figure 2, when the motor rotates in the forward direction, rotary disc 1 and rotary disc 2 rotate accordingly. At this stage, the distances from line fixation seat 1 to roller 1 and from line fixation seat 2 to roller 3 are smaller, resulting in a small oscillation amplitude of the tail fin. The diameter of the circular motion is denoted as d_1 . As the motor continues to rotate forward, the distance between roller 3 and roller 4 increases, while the distance between roller 1 and roller 2 decreases. After sliding track 1 and sliding track 2 complete a 180° rotation about their respective centers, the distance between roller 3 and roller 4 decreases and the distance between roller 1 and roller 2 increases, thus enabling the reciprocating oscillation of the tail fin. Taking the forward motor rotation as an example, the mechanism motion over one full oscillation cycle of the tail fin is illustrated in Figure 3. We mark a fixed point M on Traction Line 1 and a fixed point N on Traction Line 2. By tracking the motion of M and N , the movement of the traction lines can be clearly illustrated.

Similarly, as shown in Figure 2, when the motor rotates in the reverse direction, the distances from line fixation seat 1 to roller 1 and from line fixation seat 2 to roller 3 are larger, resulting in a large oscillation amplitude of the tail fin. The diameter of

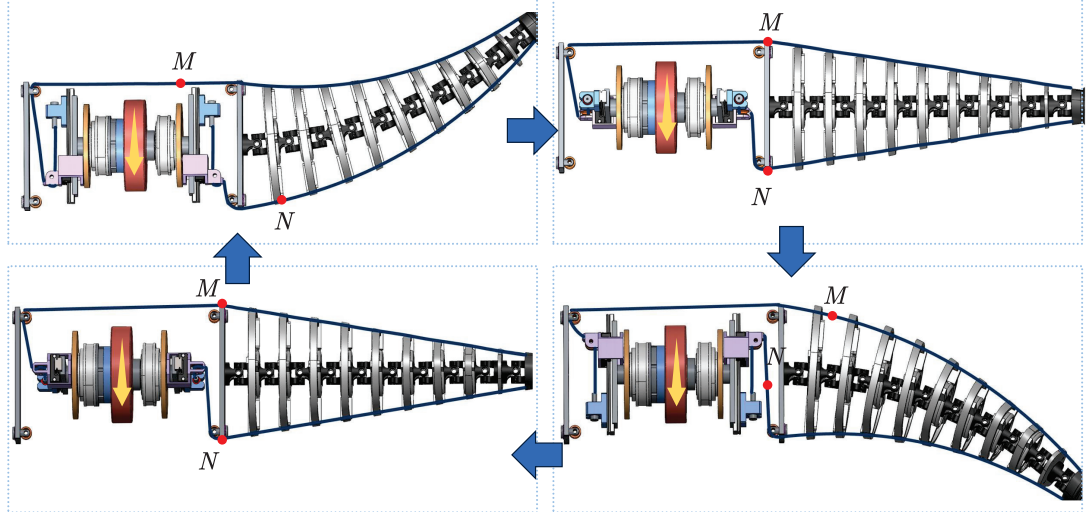


Fig. 3: Schematic diagram of the mechanism motion during one full tail-fin oscillation cycle under forward motor rotation.

the circular motion is denoted as d_2 . The oscillation mechanism during motor reversal is analogous to that during forward rotation.

3 Dynamic Modeling

3.1 Coordinate System and Variable Definitions

To facilitate the description, the robotic fish is simplified as a multi-link structure, as shown in Figure 4. Each link represents a part of the robotic fish body. Specifically, L_0 represents the head of the robotic fish, which is divided into two segments, L_{01} and L_{02} , at the location of the pectoral fins. L_i denotes the ten links forming the tail section of the robotic fish, where $i \in [1, 10]$. L_l and L_r represent the left and right pectoral fin links, respectively. L_a denotes the link corresponding to the distance between the pectoral fin mounting position and the central axis of the body. J_i represents the endpoint of each link, where $i \in \{[0, 10], l, r\}$. The inertial coordinate system is defined as $C_w = (O_w, x_w, y_w, z_w)$, where the $O_wx_wy_w$ plane coincides with the horizontal plane, and z_w is perpendicular to the $O_wx_wy_w$ plane and points outward. For L_i , a body-fixed coordinate system $C_i = (O_i, x_i, y_i, z_i)$ is established, where $i \in \{[0, 10], l, r\}$, and O_i coincides with the center of J_i . The length of L_i is denoted as l_i , where $i \in [1, 10]$. l_{01} , l_{02} , and l_a represent the lengths of L_{01} , L_{02} , and L_a , respectively. The angle of each joint J_i is represented by θ_i , where $i \in [0, 10]$. θ_0 represents the yaw angle of the head segment. θ_l and θ_r denote the rotation angles of the left and right pectoral fins about J_l and J_r , respectively. In each coordinate system, the unit vectors along the x , y , and z axes are represented by e , j , and k , respectively.

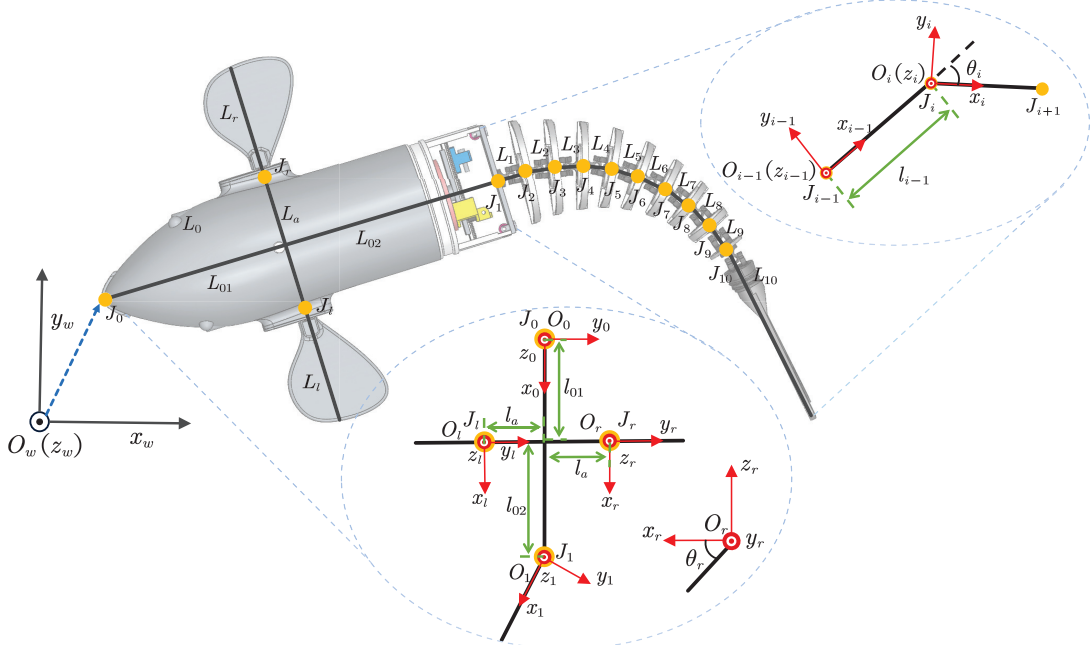


Fig. 4: Simplified joint and coordinate definition diagram of the robotic fish.

3.2 Kinematic Analysis

3.2.1 Kinematics Analysis of Wire-Driven Tail

According to Lighthill's model, the body curve of a fish swim can be expressed as follows:

$$y(x, t) = (a_0 + a_1 x + a_2 x^2) \sin [2\pi(kx - ft)] \quad (1)$$

where $y(x, t)$ is the lateral excursion of the mid-line at time t , and x is the displacement along the main axis. The amplitude envelope of lateral motion follows the quadratic function $A(x) = a_0 + a_1 x + a_2 x^2$. In this study, the coefficients a_0 , a_1 and a_2 derived from the wave amplitude of carangiform fish swimming mode[31]. k is the body wave number, f is the body wave frequency. This model has since been widely adopted as a standard formulation for describing fish swimming and for the control of robotic fish.

The tail-bending angle can be approximated using the local tangent slope, expressed as:

$$\theta(x, t) \approx \arctan\left(\frac{\partial y}{\partial x}\right) \quad (2)$$

According to the proportion of the tail region, the amplitude envelope can be written as:

$$A(x) = A_{\max} \left(\frac{x - 0.6}{0.4} \right)^2 \quad (3)$$

For a typical case with $k = 1$, the maximum bending angle at $x = 1$ (i.e., the tail tip) is 53° . This yields $A_{\max} = 0.165$. Finally, the fish-body wave model is presented as follows:

$$y(x, t) = 1.03 (x - 0.6)^2 \sin[2\pi(x - ft)] \quad (4)$$

Although a traveling-wave curvature model is widely used to describe the midline kinematics of biological fish, the curvature variation in the tail region is relatively small. Moreover, the proposed wire-driven tail mechanism with equally spaced joints and a NiTi alloy backbone inherently produces bending shapes close to a circular arc. Therefore, the constant-curvature assumption provides an appropriate and structurally consistent approximation for the tail kinematics. We sampled 20 physical positions s_i along the tail and computed the corresponding y_i values using the travelling-wave model. Using these 20 sampled points, a circular arc was fitted through a least-squares circle fitting method. The fitted circle had center $(s_c, y_c) = (0.1782, 0.2172)$ m and radius $R = 0.2572$ m. For each point, the radial deviation was computed as $e_i = \sqrt{(s_i - s_c)^2 + (y_i - y_c)^2} - R$. The RMS geometric error was $e_{RMS} = 9.93$ mm, corresponding to 3.2% of the tail length. This small error indicates that, in this study, the travelling-wave model can be well approximated by a constant-curvature model in the tail region.

We choose the constant curvature method to establish the kinematic model of the tail. The constant curvature method is based on the following assumptions: (1) The distances between adjacent tail joints of the robotic fish are equal, and the bending curve of each joint segment forms a smooth, continuous curve with equal curvature; (2) During bending, the traction lines of each joint segment are assumed to be continuous, smooth curves with equal curvature; (3) It is assumed that the nickel-titanium alloy wire running through the spine of the tail forms a constant curvature curve during the bending process.

First, the kinematic mapping relationship between the joint space and the operational space is analyzed. The base coordinate system $C_n = (O_n, x_n, y_n, z_n)$ is established with J_1 as the origin, and the end coordinate system $C_c = (O_c, x_c, y_c, z_c)$ is defined, as shown in Figure 5a. When the tail bends, the end coordinate system can be regarded as obtained by rotating the base coordinate system around the z -axis by θ . l represents the length of the nickel-titanium alloy wire, and the homogeneous transformation matrix T between the two coordinate systems is presented as follows:

$$T = \begin{bmatrix} \cos \theta & -\sin \theta & \frac{l}{\theta} \sin \theta \\ \sin \theta & \cos \theta & \frac{l}{\theta} (1 - \cos \theta) \\ 0 & 0 & 1 \end{bmatrix} \quad (5)$$

Next, the relationship between the drive space and the joint space is analyzed. Δl_1 represents the variation in traction line 1, Δl_2 represents the variation in traction line 2, and γ represents the rotation angle of the rotary disc. Based on the structure of the transmission mechanism, it is simplified to analyze the relationship between Δl_1 , Δl_2 , and γ during one complete oscillation cycle of the tail, which corresponds to one full rotation of the rotary disc. In the first and second transmission submodules, roller 2 (roller 4) is simplified as a fixed point O . G represents the positions of line fixation seat 1 (line fixation seat 2). P is the initial position of roller 1 (roller 3), as

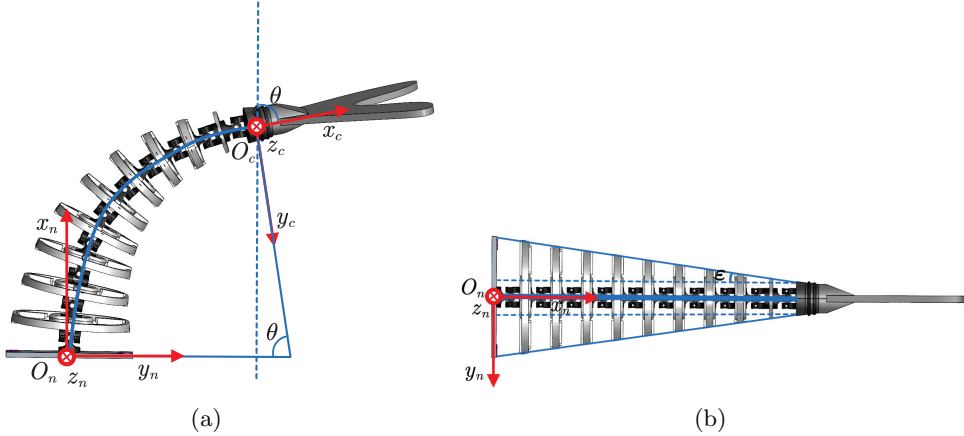


Fig. 5: Kinematic model diagram of the robotic fish tail. (a) Schematic of the tail kinematic coordinate system. (b) Top view of the tail.

shown in Figure 6a. Roller 1 (roller 3) and line fixation seat 1 (line fixation seat 2) both move in circular motion along with the rotary disc's rotation. P_1 represents the position change of roller 1 (roller 3). According to the mechanism's characteristics, the motor's rotation direction affects the circular motion's diameter d , resulting in tail oscillations with different amplitudes. When the motor rotates forward, $d_1 = 0.07\text{m}$, result in small-amplitude oscillations of the tail, with the initial state of both the first and second transmission submodules as shown in Figure 6a. The motion process of the first transmission submodule is from Figure 6b to Figure 6h, and the motion process of the second transmission submodule is from Figure 6h to Figure 6b. When the motor rotates in reverse, $d_2 = 0.1\text{m}$, result in large-amplitude oscillations of the tail, with the initial state of both the first and second transmission submodules as shown in Figure 6a. The motion process of the first transmission submodule is from Figure 6h to Figure 6b, and the motion process of the second transmission submodule is from Figure 6b to Figure 6h.

The relationship between Δl_1 , Δl_2 , and γ is expressed as follows:

$$\Delta l_1 = \begin{cases} d \cos\left(\frac{\gamma}{2} - \frac{\pi}{4}\right) - \frac{\sqrt{2}}{2}d, & 0 \leq \gamma \leq \frac{3\pi}{2} \\ d \sin\left(\frac{\gamma}{2} - \frac{3\pi}{4}\right) - \frac{\sqrt{2}}{2}d, & \frac{3\pi}{2} < \gamma \leq 2\pi \end{cases} \quad (6)$$

$$\Delta l_2 = \begin{cases} d \sin\left(\frac{\pi}{4} - \frac{\gamma}{2}\right) - \frac{\sqrt{2}}{2}d, & 0 \leq \gamma \leq \frac{\pi}{2} \\ d \sin\left(\frac{\gamma}{2} - \frac{\pi}{4}\right) - \frac{\sqrt{2}}{2}d, & \frac{\pi}{2} < \gamma \leq 2\pi \end{cases} \quad (7)$$

As shown in Figure 7, it should be noted that during the motion process $|\Delta l_1| \neq |\Delta l_2|$, the actual traction line variation Δl affecting θ is expressed as $|\Delta l| = \min\{|\Delta l_1|, |\Delta l_2|\}$, that is as follows:

$$\Delta l = \begin{cases} \Delta l_1, & 0 \leq \gamma < \pi \\ -\Delta l_2, & \pi \leq \gamma \leq 2\pi \end{cases} \quad (8)$$

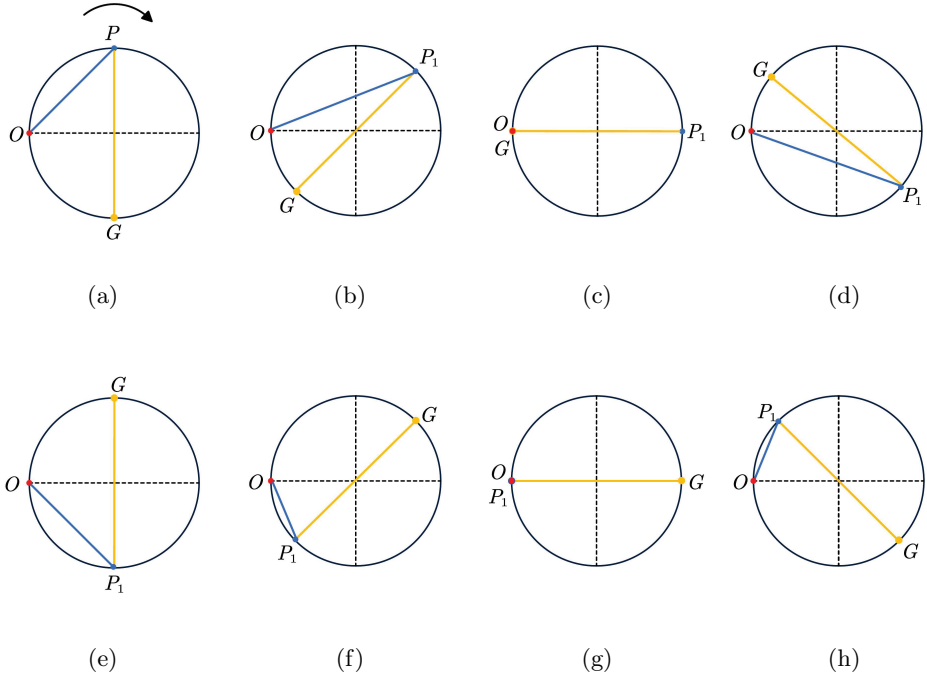


Fig. 6: Schematic of traction line variation in the transmission submodule during one motor rotation cycle. (a) Initial state of the transmission submodule. (b)–(h) Motion process of the transmission submodule.

Its final form is as follows:

$$\Delta l = \left(d - \frac{\sqrt{2}}{2} d \right) \sin \gamma \quad (9)$$

$$\cos \varepsilon \cdot \Delta l = (\rho - \rho_1) \theta, \quad \rho - \rho_1 = a \quad (10)$$

In the above expression, a denotes the parameter to be identified, and $\cos \varepsilon \cdot \Delta l$ represents the projection of the traction line variation along the spine direction, as shown in Figure 5b. ρ and ρ_1 respectively represent the radius of curvature of the nickel-titanium alloy wire and the traction line when they are bent. Accordingly, the mapping from the drive space to the joint space is given by:

$$\theta = \frac{\cos \varepsilon \left(d - \frac{\sqrt{2}}{2} d \right)}{a} \sin \gamma \quad (11)$$

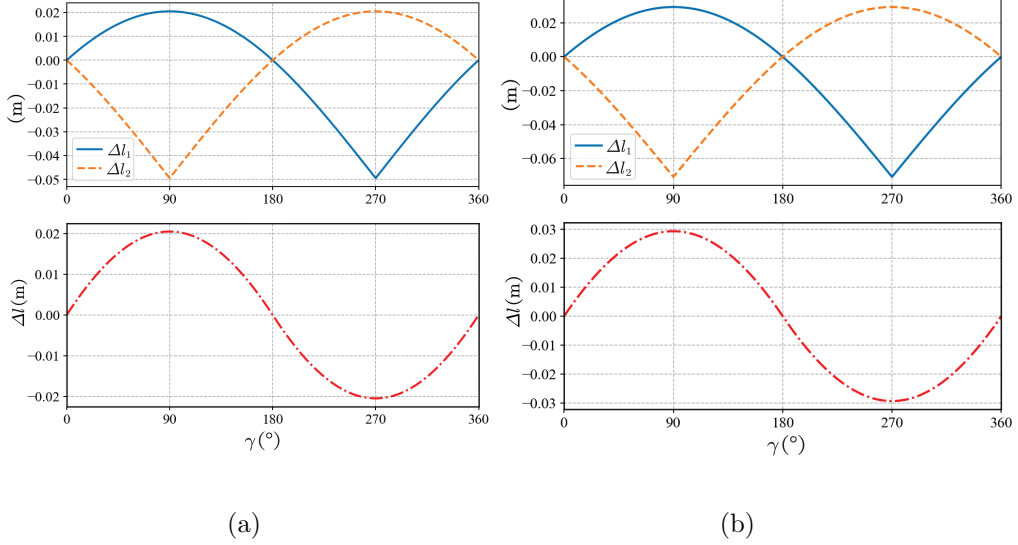


Fig. 7: Schematic diagram of the relationship between Δl , Δl_1 , Δl_2 and γ . (a) Motor rotating forward, small-amplitude tail fin oscillation. (b) Motor rotating in reverse, large-amplitude tail fin oscillation.

3.2.2 Kinematic Analysis of the Trunk

According to the structural characteristics of the robotic fish trunk, the rotation matrix and position vector of coordinate system C_i relative to C_{i-1} are as follows:

$${}^{i-1}\mathbf{R}_i = \begin{pmatrix} \cos \theta_i & -\sin \theta_i & 0 \\ \sin \theta_i & \cos \theta_i & 0 \\ 0 & 0 & 1 \end{pmatrix}, \quad {}^{i-1}\mathbf{P}_i = \begin{pmatrix} l_{i-1} \\ 0 \\ 0 \end{pmatrix} \quad (12)$$

Meanwhile, ${}^i\mathbf{R}_{i-1} = {}^{i-1}\mathbf{R}_i^T$, T denotes the transpose.

The velocity relationship between adjacent links in the trunk of the robotic fish is given as follows:

$$\begin{cases} \mathbf{V}_i = \begin{pmatrix} \mathbf{U}_i \\ \boldsymbol{\Omega}_i \end{pmatrix} = {}^i\mathbf{H}_{i-1}\mathbf{V}_{i-1} + \dot{\theta}_i \mathbf{K}_i \\ {}^i\mathbf{H}_{i-1} = \begin{pmatrix} {}^i\mathbf{R}_{i-1} & {}^i\mathbf{R}_{i-1}^T \hat{\mathbf{P}}_i \\ 0_{3 \times 3} & {}^i\mathbf{R}_{i-1} \end{pmatrix} \end{cases} \quad (13)$$

where \mathbf{V}_i denotes the (6×1) dimensional velocity vector of L_i in coordinate system C_i , \mathbf{U}_i denotes the (3×1) dimensional linear velocity vector of L_i , $\boldsymbol{\Omega}_i$ denotes the (3×1) dimensional angular velocity vector of L_i , $\mathbf{K}_i = [0_{3 \times 1}^T, k_i^T]^T$ represents a (6×1) dimensional unit vector, ${}^i\mathbf{H}_{i-1}$ represents the (6×6) dimensional transformation matrix, and \hat{a} denotes the (3×3) dimensional skew-symmetric matrix corresponding to the vector a .

By differentiating the velocity relationship, the acceleration relationship between adjacent links in the trunk of the robotic fish is obtained:

$$\begin{cases} \dot{\mathbf{V}}_i = {}^i \mathbf{H}_{i-1} \dot{\mathbf{V}}_{i-1} + \boldsymbol{\xi}_i + \ddot{\theta}_i \mathbf{K}_i \\ \boldsymbol{\xi}_i = \left(\begin{array}{c} [{}^i \mathbf{R}_{i-1} (\mathbf{U}_{i-1} - {}^{i-1} \mathbf{P}_i \times \boldsymbol{\Omega}_{i-1})] \times \dot{\theta}_i \mathbf{k}_i \\ ({}^i \mathbf{R}_{i-1} \boldsymbol{\Omega}_{i-1}) \times \dot{\theta}_i \mathbf{k}_i \end{array} \right) \end{cases} \quad (14)$$

Accordingly, if \mathbf{V}_0 , $\dot{\mathbf{V}}_0$ and $\{(\theta_i, \dot{\theta}_i, \ddot{\theta}_i) \mid i \in [1, n]\}$ are known, the velocity and acceleration of each link can be calculated. Since a planar dynamic model of the robotic fish is to be established, the pitch angle and roll angle are set to 0. Thus, the transformation relationships between \mathbf{V}_0 and $\dot{\mathbf{V}}_0$ in coordinate systems C_0 and C_w are given by:

$$\begin{cases} {}^w \mathbf{V}_0 = {}^w \mathbf{H}_0 \mathbf{V}_0 \\ {}^w \dot{\mathbf{V}}_0 = {}^w \mathbf{H}_0 \dot{\mathbf{V}}_0 + \begin{pmatrix} {}^w \boldsymbol{\Omega}_0 \times {}^w \mathbf{U}_0 \\ 0_{3 \times 1} \end{pmatrix} \end{cases} \quad (15)$$

where ${}^w \mathbf{H}_0 = \begin{pmatrix} {}^w \mathbf{R}_0 & 0_{3 \times 3} \\ 0_{3 \times 3} & \mathbf{I}_{3 \times 3} \end{pmatrix}$.

3.2.3 Kinematic Analysis of the Pectoral Fins

As shown in Figure 4, the rotation matrix and position vector of the left pectoral fin coordinate system C_l relative to the head coordinate system C_0 are as follows:

$$\begin{cases} {}^0 \mathbf{R}_l = \begin{pmatrix} \cos \theta_l & 0 & \sin \theta_l \\ 0 & 1 & 0 \\ -\sin \theta_l & 0 & \cos \theta_l \end{pmatrix} \\ \mathbf{P}_l = \begin{pmatrix} l_{01} \\ -l_a \\ 0 \end{pmatrix} \end{cases} \quad (16)$$

Similarly, the rotation matrix and position vector of the right pectoral fin coordinate system C_r relative to the head coordinate system C_0 are as follows:

$$\begin{cases} {}^0 \mathbf{R}_r = \begin{pmatrix} \cos \theta_r & 0 & \sin \theta_r \\ 0 & 1 & 0 \\ -\sin \theta_r & 0 & \cos \theta_r \end{pmatrix} \\ \mathbf{P}_r = \begin{pmatrix} l_{01} \\ l_a \\ 0 \end{pmatrix} \end{cases} \quad (17)$$

The velocity relationship between C_r and C_0 is given as follows:

$$\begin{cases} \mathbf{V}_r = {}^r \mathbf{H}_0 \mathbf{V}_0 + \dot{\theta}_r \mathbf{Z} \\ {}^r \mathbf{H}_0 = \begin{pmatrix} {}^r \mathbf{R}_0 & -{}^r \mathbf{R}_0^0 \hat{\mathbf{P}}_r \\ 0_{3 \times 3} & {}^r \mathbf{R}_0 \end{pmatrix} \end{cases} \quad (18)$$

where ${}^r\mathbf{R}_0 = {}^0\mathbf{R}_r^T$, ${}^r\mathbf{H}_0$ is the transformation matrix, $\mathbf{Z} = (0_{1 \times 5} \ 1)$.

By differentiating the velocity relationship, the acceleration relationship between C_r and C_0 is obtained as follows:

$$\begin{cases} \dot{\mathbf{V}}_r = {}^r\mathbf{H}_0 \dot{\mathbf{V}}_0 + \boldsymbol{\eta}_r + \ddot{\theta}_r \mathbf{Z} \\ \boldsymbol{\eta}_r = \left(\begin{array}{c} \dot{\theta}_r {}^r\mathbf{R}_0 (\mathbf{j}_r \times (\mathbf{U}_0 - {}^0\mathbf{P}_r \times \boldsymbol{\Omega}_0)) \\ \dot{\theta}_r {}^r\mathbf{R}_0 (\mathbf{j}_r \times \boldsymbol{\Omega}_0) \end{array} \right) \end{cases} \quad (19)$$

Similarly, the velocity and acceleration relationships between C_l and C_0 are given as follows:

$$\begin{cases} \mathbf{V}_l = {}^l\mathbf{H}_0 \mathbf{V}_0 + \dot{\theta}_l \mathbf{Z} \\ {}^l\mathbf{H}_0 = \begin{pmatrix} {}^l\mathbf{R}_0 & -{}^l\mathbf{R}_0^0 \hat{\mathbf{P}}_l \\ 0_{3 \times 3} & {}^l\mathbf{R}_0 \end{pmatrix} \\ \dot{\mathbf{V}}_l = {}^l\mathbf{H}_0 \dot{\mathbf{V}}_0 + \boldsymbol{\eta}_l + \ddot{\theta}_l \mathbf{Z} \\ \boldsymbol{\eta}_l = \left(\begin{array}{c} \dot{\theta}_l {}^l\mathbf{R}_0 (\mathbf{j}_l \times (\mathbf{U}_0 - {}^0\mathbf{P}_l \times \boldsymbol{\Omega}_0)) \\ \dot{\theta}_l {}^l\mathbf{R}_0 (\mathbf{j}_l \times \boldsymbol{\Omega}_0) \end{array} \right) \end{cases} \quad (20)$$

Accordingly, if \mathbf{V}_0 , $\dot{\mathbf{V}}_0$, $(\theta_l \ \dot{\theta}_l \ \ddot{\theta}_l)$ and $(\theta_r \ \dot{\theta}_r \ \ddot{\theta}_r)$ are known, the velocity and acceleration of the left and right pectoral fins can be calculated.

3.3 Hydrodynamic Analysis

The hydrodynamic analysis of the trunk is performed using the Morrison equation and the Strip method. The hydrodynamic forces primarily consist of added mass forces and drag. The added mass force is the reaction force exerted by fluid inertia on an object in an inviscid potential flow, while the drag is the reaction force exerted by the water on the fish body during its movement in the water. The hydrodynamic force \mathbf{F}_i acting on the L_i is given by:

$$\mathbf{F}_i = -\mathbf{M}_{ad,i} \dot{\mathbf{V}}_i - \boldsymbol{\gamma}_{ad,i} + \mathbf{f}_{dr,i} \quad (21)$$

where $\mathbf{M}_{ad,i}$ is the added inertia matrix of L_i . $\boldsymbol{\gamma}_{ad,i}$ are the Coriolis and centripetal forces induced by the added inertia. $\mathbf{f}_{dr,i}$ is the drag force. $\mathbf{M}_{ad,i}$ depends on the dimensionless added inertia coefficient $c_{m,i}$. $\mathbf{f}_{dr,i}$ depends on the dimensionless friction coefficient $c_{f,i}$ and the drag coefficient $c_{d,i}$.

The hydrodynamic analysis of the pectoral fins is performed using a quasi-steady lift-drag model. The left and right pectoral fins are similar; taking the right pectoral fin as an example, the velocity coordinate system $C_{rv} = (O_{rv}, x_{rv}, y_{rv}, z_{rv})$ being introduced, the hydrodynamic force and moment acting on the right pectoral fin are as follows:

$$\begin{pmatrix} \mathbf{F}_r \\ \boldsymbol{\tau}_r \end{pmatrix} = \begin{pmatrix} {}^r\mathbf{R}_{rv}^{rv} \mathbf{F}_r \\ {}^r\mathbf{R}_{rv}^{rv} \boldsymbol{\tau}_r \end{pmatrix} \quad (22)$$

$$\begin{cases} {}^{rv}\mathbf{F}_r = \frac{1}{2}\rho S_r \mathbf{V}_r^T \mathbf{V}_r \begin{pmatrix} -C_{D,r}(\alpha_r) \\ C_{S,r}(\beta_r) \\ -C_{L,r}(\alpha_r) \end{pmatrix} \\ {}^{rv}\boldsymbol{\tau}_r = \frac{1}{2}\rho S_r \mathbf{V}_r^T \mathbf{V}_r \begin{pmatrix} C_{\tau x,r}(\alpha_r) \\ C_{\tau y,r}(\beta_r) \\ C_{\tau z,r}(\alpha_r) \end{pmatrix} + N_r \boldsymbol{\Omega}_r \end{cases} \quad (23)$$

where ρ is the fluid density, S_r is the reference area of the pectoral fin, $C_{D,r}$, $C_{S,r}$, $C_{L,r}$, $C_{\tau x,r}$, $C_{\tau y,r}$, and $C_{\tau z,r}$ are the hydrodynamic coefficients related to the angle of attack α_r and the sideslip angle β_r , while N_r is the rotational damping coefficient.

3.4 Newton–Euler Dynamic Modeling

The dynamics of the robotic fish are analyzed using the Newton-Euler method. The resultant forces acting on each link of the robotic fish and the corresponding dynamic equations are as follows:

$$\begin{cases} \mathbf{M}_0 \dot{\mathbf{V}}_0 = \mathbf{F}_0 - \boldsymbol{\gamma}_0 - {}^0\mathbf{H}_1^1 \mathbf{G}_{0,1} - {}^0\mathbf{H}_r^r \mathbf{G}_{0,r} - {}^0\mathbf{H}_l^l \mathbf{G}_{0,l} \\ \mathbf{M}_i \dot{\mathbf{V}}_i = \mathbf{F}_i - \boldsymbol{\gamma}_i + {}^i\mathbf{G}_{i-1,i} - {}^i\mathbf{H}_{i+1}^{i+1} \mathbf{G}_{i,i+1} \quad (i = 1, 2, 3, \dots, 10) \\ \mathbf{M}_l \dot{\mathbf{V}}_l = \begin{pmatrix} \mathbf{F}_l \\ \boldsymbol{\tau}_l \end{pmatrix} + {}^l\mathbf{G}_{0,l} - \boldsymbol{\gamma}_l \\ \mathbf{M}_r \dot{\mathbf{V}}_r = \begin{pmatrix} \mathbf{F}_r \\ \boldsymbol{\tau}_r \end{pmatrix} + {}^r\mathbf{G}_{0,r} - \boldsymbol{\gamma}_r \end{cases} \quad (24)$$

where \mathbf{M}_i is the inertia matrix of L_i , as follows:

$$\mathbf{M}_i = \begin{pmatrix} m_i \mathbf{I}_{3 \times 3} & -c_i m_i \hat{\mathbf{e}}_i \\ c_i m_i \hat{\mathbf{e}}_i & c_i^2 m_i \hat{\mathbf{e}}_i^T \hat{\mathbf{e}}_i + \mathbf{I}_i \end{pmatrix} \quad (25)$$

m_i is the mass of L_i , c_i represents the distance between O_i and the center of mass of L_i , \mathbf{I}_i is the moment of inertia relative to the center of mass, $\boldsymbol{\gamma}_i$ is the Coriolis and centripetal forces acting on L_i :

$$\boldsymbol{\gamma}_i = \begin{pmatrix} m_i \hat{\boldsymbol{\Omega}}_i & -c_i m_i \hat{\boldsymbol{\Omega}}_i \hat{\mathbf{e}}_i \\ c_i m_i \hat{\boldsymbol{\Omega}}_i \hat{\mathbf{e}}_i & \hat{\boldsymbol{\Omega}}_i (c_i^2 m_i \hat{\mathbf{e}}_i^T \hat{\mathbf{e}}_i + \mathbf{I}_i) \end{pmatrix} \mathbf{V}_i \quad (26)$$

${}^i\mathbf{G}_{i-1,i}$ is the force exerted by L_{i-1} on L_i in C_i .

Due to ${}^{11}G_{10,11} = 0$, the dynamic equation of the robotic fish head is obtained by recursively deriving the relationship between the links, as follows:

$$\begin{cases} {}^0\mathbf{M}_{body} \dot{\mathbf{V}}_0 = {}^0\mathbf{f}_{dr,body} - {}^0\boldsymbol{\gamma}_{body} - {}^0\mathbf{T}_{body} - {}^0\mathbf{G}_{0,r} - {}^0\mathbf{G}_{0,l} \\ {}^0\mathbf{M}_{body} = \sum_{i=0}^n [{}^i\mathbf{H}_0^T (\mathbf{M}_i + \mathbf{M}_{ad,i}) {}^i\mathbf{H}_0] \\ {}^0\mathbf{f}_{dr,body} = \sum_{i=0}^n {}^i\mathbf{H}_0^T \mathbf{f}_{dr,i} \\ {}^0\boldsymbol{\gamma}_{body} = \sum_{i=0}^n {}^i\mathbf{H}_0^T (\boldsymbol{\gamma}_i + \boldsymbol{\gamma}_{ad,i}) \\ {}^0\mathbf{T}_{body} = \sum_{i=1}^n {}^i\mathbf{H}_0^T (\mathbf{M}_i + \mathbf{M}_{ad,i}) \sum_{j=1}^i {}^i\mathbf{H}_j (\boldsymbol{\xi}_j + \ddot{\theta}_j \mathbf{K}_j) \\ {}^0\mathbf{G}_{0,r} = {}^0\mathbf{H}_r^r \mathbf{G}_{0,r} \\ {}^0\mathbf{G}_{0,l} = {}^0\mathbf{H}_l^l \mathbf{G}_{0,l} \end{cases} \quad (27)$$

where ${}^i\mathbf{H}_0 = {}^i\mathbf{H}_{i-1}^{i-1} \mathbf{H}_{i-2} \cdots {}^1\mathbf{H}_0$, ${}^i\mathbf{H}_i = \mathbf{I}_{6 \times 6}$.

3.5 Hydrodynamic Parameter Identification

We use a data-driven approach to identify the hydrodynamic parameters, treating the established dynamic model as a gray-box model. Hydrodynamic parameter identification is performed using the actual motion data of the robotic fish. λ is the set of hydrodynamic parameters, as follows:

$$\lambda = \{(c_{m,i}, c_{d,i}, c_{f,i}) \mid i \in [0, 10]\} \quad (28)$$

The differential evolution algorithm is used for global optimization of the parameters, with the objective function set as the residual sum of squares (RSS) between the simulated and experimental speeds. The specific form is as follows:

$$\arg \min_{\lambda} \sum_{i=1}^N [100 \cdot (v_e(i) - v_s(i))]^2 \quad \text{s.t. } \lambda_l \leq \lambda \leq \lambda_u \quad (29)$$

where $v_e(i)$ is the i -th experimental speed, $v_s(i)$ is the i -th simulated speed, N is the number of data points, and the constant 100 converts the velocity unit from (m/s) to (cm/s) to enhance the identification sensitivity. λ_l and λ_u represent the lower and upper bounds of λ , respectively. The differential evolution algorithm initializes the search by randomly generating a population of candidate solutions and evaluates each individual based on its fitness value, which serves as the selection criterion. The algorithm primarily consists of mutation, crossover, and selection steps. The main process is detailed in Algorithm 1 using pseudo-code.

4 Simulation and Experimental Results

4.1 Kinematic Parameter Identification and Validation of Wire-Driven Tail

To obtain a kinematic model of the robotic fish tail that closely fits the actual motion, we use data from real-motion experiments to identify the model parameters a . We

Algorithm 1 Differential Evolution for Hydrodynamic Parameter Identification

- 1: **Initialization:** Randomly generate the initial population $P^{(0)} = \{\lambda_1^{(0)}, \lambda_2^{(0)}, \dots, \lambda_M^{(0)}\}$, where each individual λ_k is a 15-dimensional hydrodynamic parameter vector.
- 2: **Evaluate fitness:** For each individual λ_k , compute the objective function

$$J(\lambda_k) = \sum_{i=1}^N [100(v_e(i) - v_s(i; \lambda_k))]^2,$$

where $v_e(i)$ and $v_s(i; \lambda_k)$ are the i -th experimental and simulated velocities, respectively.

- 3: **for** $t = 1$ to T **do**
- 4: **for** $k = 1$ to M **do**
- 5: Randomly select three distinct indices $r_1, r_2, r_3 \in \{1, 2, \dots, M\} \setminus \{k\}$.
- 6: **Mutation:**

$$v_k = \lambda_{r_1} + F(\lambda_{r_2} - \lambda_{r_3}).$$
- 7: **Crossover:** For each dimension j of the vector, generate the trial vector u_k as

$$u_{k,j} = \begin{cases} v_{k,j}, & \text{if rand} < CR, \\ \lambda_{k,j}, & \text{otherwise,} \end{cases}$$

where rand is a uniformly distributed random number in $(0, 1)$.
- 8: Evaluate the fitness $J(u_k)$.
- 9: **if** $J(u_k) < J(\lambda_k)$ **then**
- 10: $\lambda_k \leftarrow u_k$.
- 11: **end if**
- 12: **end for**
- 13: **if** the termination criterion is satisfied **then**
- 14: **break**
- 15: **end if**
- 16: **end for**
- 17: **Output:** Select the individual with the smallest fitness as the optimal hydrodynamic parameters:

$$\lambda^* = \arg \min_{\lambda_k \in P} J(\lambda_k).$$

vary the rotation angle of the rotary disc from 0° to 360° , with an interval of 30° . We take 12 sets of actual measurement values of θ . The optimal value of a is estimated using the least squares method, as given by the following equations:

$$\theta = k \sin \gamma \quad (30)$$

$$J(k) = \min \sum_{j=1}^{12} (\theta_j - k \sin \gamma)^2 \quad (31)$$

$$a = \frac{\cos \varepsilon \left(d - \frac{\sqrt{2}}{2} d \right)}{k} \quad (32)$$

The identification results are shown in Table 2. When the motor rotates forward, $d_1 = 0.07\text{m}$, $a_1 = 0.0401\text{m}$, $R^2 = 0.998$, and $RMSE = 0.017$; when the motor rotates in reverse, $d_2 = 0.1\text{m}$, $a_2 = 0.0325\text{m}$, $R^2 = 0.997$, and $RMSE = 0.036$. The fitting results of the tail kinematic model are shown in Figure 8. When the motor rotates forward, the tail fin oscillates with a small amplitude, and the maximum tail bending angle θ_{\max} is 30° . When the motor rotates in reverse, the tail fin oscillates with a large amplitude, and the maximum tail bending angle θ_{\max} is 53° .

Table 2: Kinematic model parameters.

Parameter	l	ε	d_1	d_2	a_1	a_2
value	300 mm	0.1309	0.07 m	0.1 m	0.0401 m	0.0325 m

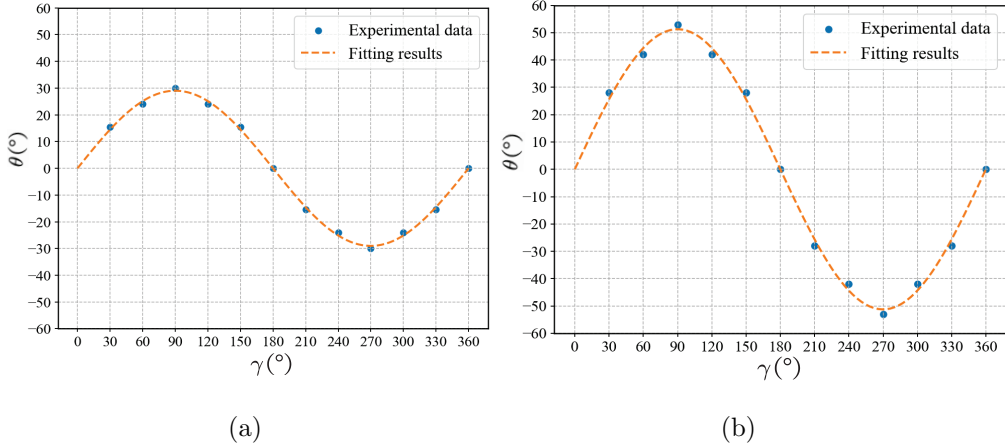


Fig. 8: Schematic diagram of the relationship between θ and γ . (a) Motor rotating forward, small-amplitude tail fin oscillation. (b) Motor rotating in reverse, large-amplitude tail fin oscillation.

4.2 Dynamic Model Identification

In this section, the underwater experiments were conducted in a pool of size $3\text{m} \times 2\text{m} \times 0.8\text{m}$. A global camera was suspended above the pool to measure the motion of the robotic fish. The speed was measured using color markers on the robotic fish, with the detailed method described in [8]. The physical parameters of each link can be easily measured or calculated using SolidWorks, as shown in Table 3. During the

hydrodynamic parameter identification, considering that the geometric shapes of segments L_1-L_3 , L_4-L_6 , and L_7-L_9 are similar within each group and all are covered by skin, we assume that the links in each group share the same hydrodynamic parameters. Therefore, there are 15 parameters to be identified in the dynamic model. Swimming experiments were conducted under different control parameters, and the speed was measured using the global vision measurement system. The differential evolution algorithm was used for parameter identification. The optimization boundaries $[\lambda_{\min}, \lambda_{\max}]$ and initial values of the hydrodynamic parameter λ_0 were set, and the identified hydrodynamic parameters λ^* are shown in Table 4.

Table 3: Physical parameters of each link of the robotic fish.

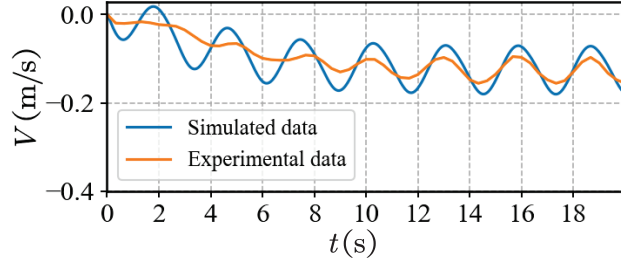
Items	Unit	L_0	L_1	L_2	L_3	L_4	L_5	L_6	L_7	L_8	L_9	L_{10}
m_i	kg	5.043	0.138	0.130	0.126	0.119	0.113	0.108	0.103	0.093	0.066	0.209
l_i	m	0.467	0.031	0.031	0.031	0.031	0.031	0.031	0.031	0.031	0.031	0.137
c_i	m	0.198	0.021	0.021	0.021	0.021	0.021	0.021	0.018	0.015	0.012	0.099
$I_{i,z}$	$\text{kg} \cdot \text{m}^2 (\times 10^{-4})$	967	29	27	26	25	24	23	22	21	15	12

Table 4: Hydrodynamic parameters of the dynamic model.

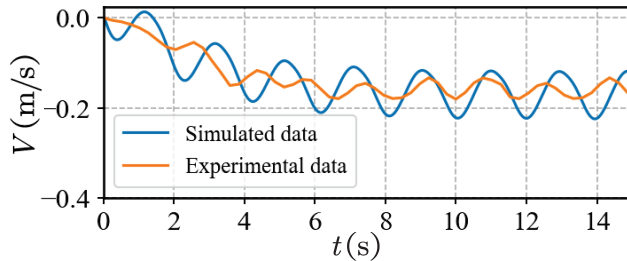
Items	λ_{\min}	λ_{\max}	λ_0	λ^*
$c_{m,0}$	0.01	2	0.01	1.90292
$c_{m,1-3}$	0.01	2	0.07	1.89993
$c_{m,4-6}$	0.01	2	0.07	0.83232
$c_{m,7-9}$	0.01	2	0.07	1.04443
$c_{m,10}$	0.01	2	0.06	0.19207
$c_{d,0}$	0.1	5	4	1.54479
$c_{d,1-3}$	0.1	5	1.5	1.59628
$c_{d,4-6}$	0.1	5	1.5	1.04258
$c_{d,7-9}$	0.1	5	1.5	1.98965
$c_{d,10}$	0.1	5	2.5	4.76729
$c_{f,0}$	0.001	1	0.02	0.96113
$c_{f,1-3}$	0.001	1	0.02	0.59210
$c_{f,4-6}$	0.001	1	0.02	0.36402
$c_{f,7-9}$	0.001	1	0.02	0.65396
$c_{f,10}$	0.001	1	0.02	0.69602

4.3 Simulation and Test of Swimming

To validate the proposed dynamic model and the estimated model parameters, the forward velocity V is discussed in detail. The model output is compared with the experimentally measured data, as shown in Figure 9. The simulated data and experimental data match well during steady swimming.



(a)



(b)

Fig. 9: Comparison of the experimental data and simulated data of dynamic model. (a) Small-amplitude tail fin oscillation, $d_1 = 0.07$ m, $w = 3.6$ rad/s. (b) Large-amplitude tail fin oscillation, $d_2 = 0.1$ m, $w = 4.1$ rad/s.

We compare the mean velocity output from the model during steady state with the mean data measured experimentally, resulting in 22 sets of comparisons between simulated data and experimental data for different rotational speeds of the rotary disc w and different tail fin oscillation amplitudes. The comparison is shown in Figure 10a. The forward velocity V increases as w . The negative sign of V simply represents the direction, which is caused by the coordinate system definition. The experimental data show that when $w > 12.9$ rad/s, the forward velocity V of the robotic fish with small-amplitude oscillation is higher than that with large-amplitude oscillation at the same w . The essential reason for this phenomenon is that the variation in the traction line caused by large-amplitude oscillation is greater than that caused by small-amplitude oscillation. When w is too high, the traction line return for large-amplitude oscillation is not completed before the rotary disc enters the next rotation cycle, leading to insufficient tail movement. As a result, the experimental forward velocity V is lower than simulated data and may even be surpassed by the small-amplitude velocity. On the other hand, small-amplitude oscillation, with its smaller traction line variation, avoids this issue. We found that when $w > 10$ rad/s, the forward velocity V for large-amplitude oscillation starts to increase more slowly and gradually stabilizes. This is mainly because large-amplitude oscillation causes larger surface waves, and the interaction of the waves with the pool wall negatively impacts the swimming of the robotic fish. Additionally, the limited space of the pool restricts the

high-speed movement of the robotic fish. The forward velocity error V_{error} between the simulated data and experimental data under different rotational speeds of the rotary disc w and different tail fin oscillation amplitudes is shown in Figure 10b. Overall, the experimental results align well with the simulation results, indicating that the dynamic model is accurate and effective in most cases. Furthermore, the mean absolute error (MAE) of the dynamic model is 0.0224m/s, and the root mean square error (RMSE) is 0.0282m/s.

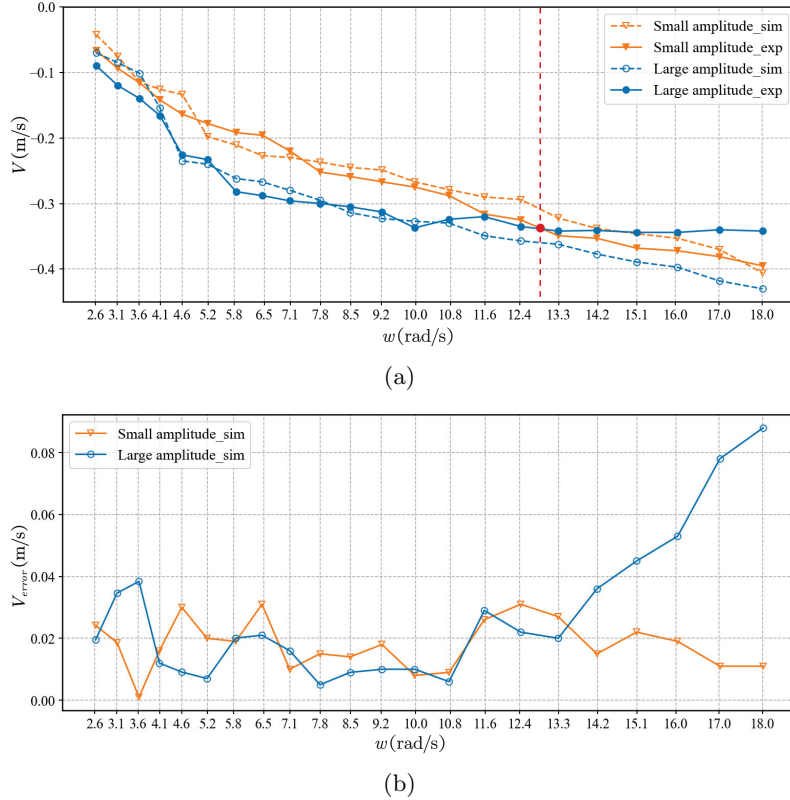


Fig. 10: Comparison of the experimental data and simulated data of the dynamic model under different caudal fin oscillation amplitudes. (a) Comparison of simulated and experimental forward velocity V ; (b) The forward velocity error V_{error} under different w and oscillation amplitudes.

The swimming simulation and experiments primarily include cruising and turning. Before the swimming tests, the robotic fish was placed in the pool, and its buoyancy and posture were adjusted to ensure it was partially submerged and maintained a horizontal position. In the cruising experiment, we measured the velocity of the robotic fish under different control parameters. The cruising process is shown in Figure 11a.

Figure 11b presents one of the cruising simulations. V_x and V_y represent the components of V_0 along the x_0 -axis and y_0 -axis, respectively. V_w denotes the yaw angular velocity of the head. In the turning test, due to the limited recording range of the camera and the pool space, we were unable to capture the complete trajectory. Figure 12a shows the turning process of the robotic fish. Figure 12b shows one of the turning simulations.

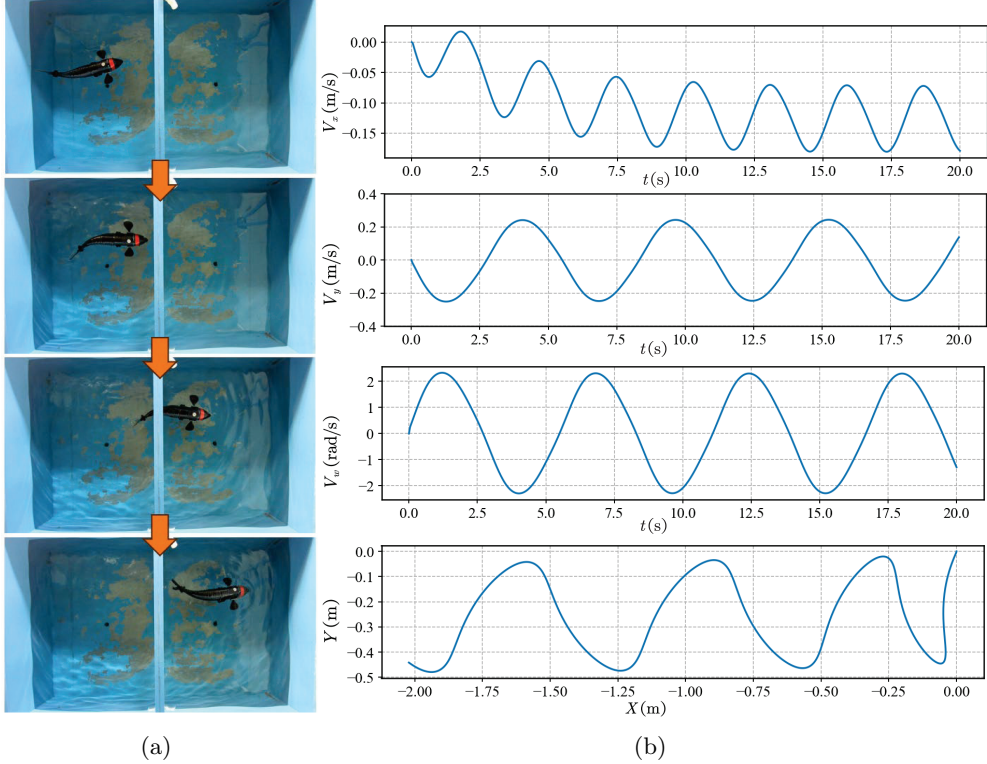


Fig. 11: Process of the cruising. (a) Cruising of the robotic fish. (b) One of the cruising simulations.

To further evaluate the performance of the robotic fish, we examined the Strouhal number and the cost of transport (COT). Strouhal number is given by:

$$St = \frac{fA}{U} \quad (33)$$

where f is the frequency, A is the peak-to-peak amplitude, and U is the forward swimming speed. We evaluated six sets of conditions with different rotational speeds of the rotary disc w and two tail-fin oscillation amplitudes, and the results are presented in Figure 13a. From the figure, it can be observed that when the robotic fish swims

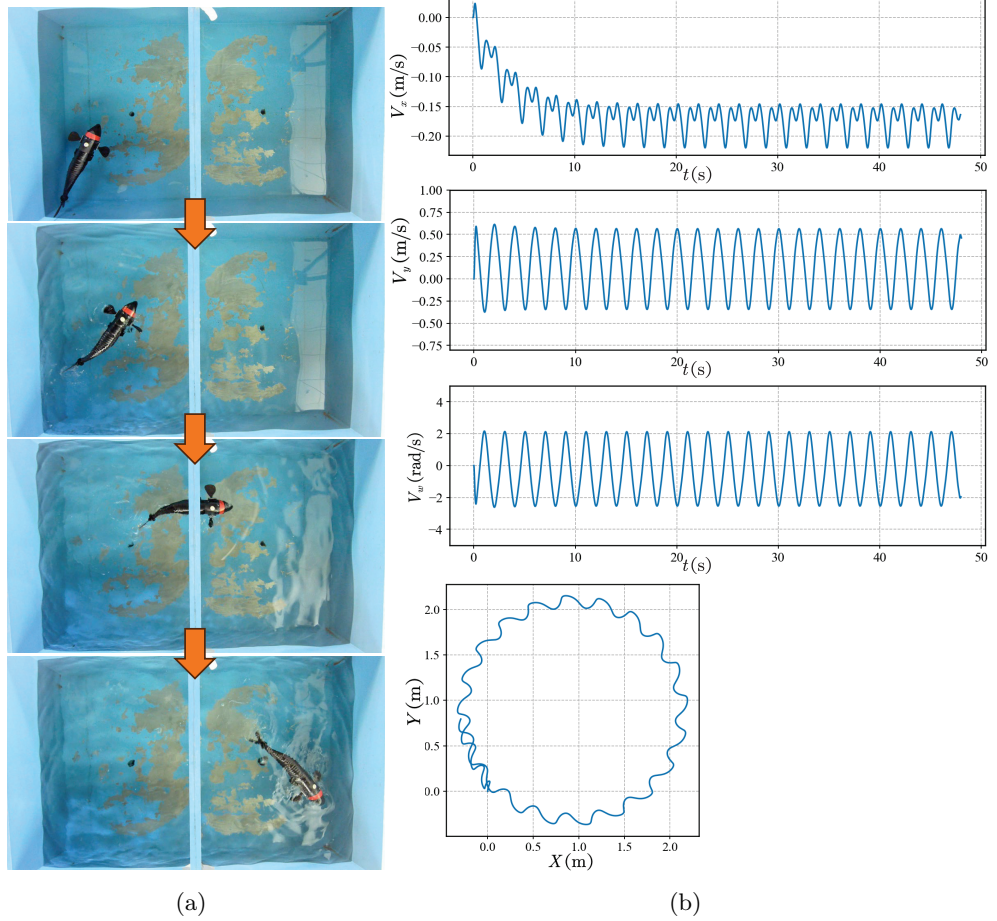


Fig. 12: Process of the turning. (a) Turning of the robotic fish. (b) One of the turning simulations.

with the small-amplitude mode, its Strouhal number falls within the interval $0.4 < St < 0.6$. Under the large-amplitude mode, the Strouhal number lies within $0.6 < St < 1.0$. Most aquatic animals exhibit Strouhal numbers within a narrow range between 0.2 and 0.4, where propulsive efficiency is typically high[32, 33]. Thus, the Strouhal number is commonly used as a qualitative indicator of swimming efficiency. Based on this criterion, the small-amplitude mode of our robotic fish operates closer to the efficient biological range between 0.2 and 0.4. Moreover, two sets of data reported for other robotic fishes fall within the intervals $0.8 < St < 1.6$ and $0.69 < St < 0.97$, respectively, which indicate that our robot fish performs better[34, 35].

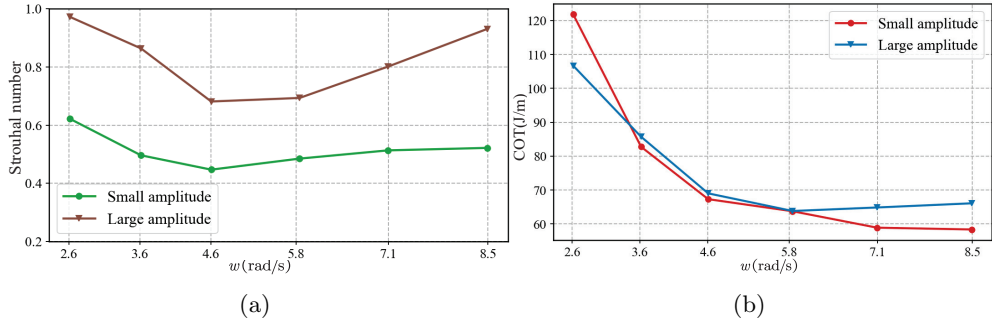


Fig. 13: Swimming performance of the robotic fish under different operating conditions. (a) Strouhal number. (b) COT.

COT is frequently applied as an index for evaluating energy consumption and its value can be obtained using the following formula:

$$COT = \frac{P}{U} \quad (34)$$

where P denotes the consumed power, and U is the swimming speed. From Figure 13b, it can be observed that the COT decreases with the increases of w , indicating an enhancement in propulsive efficiency. Meanwhile, the rate at which the COT decreases slows down as w continues to rise. This trend is consistent with observations reported for other types of robotic fish[36, 37].

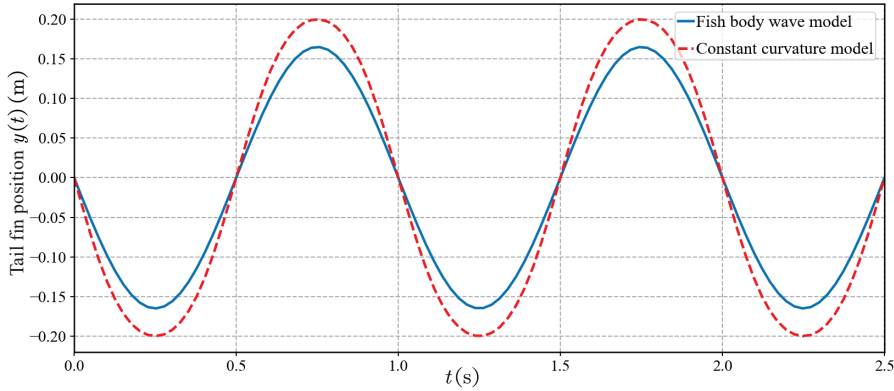


Fig. 14: Comparison of fish body wave at tail fin position.

In addition, to validate the kinematic performance of the model, we compared its tail fin motion with that of the fish body wave model. Figure 14 shows the tail fin motion waveforms of both models over the same time period. The results demonstrate that the constant curvature model effectively simulates the tail fin motion of the fish

body wave, with minimal error compared to the fish body wave model, providing strong evidence for the model's validity and effectiveness.

5 Field Experimental Validation

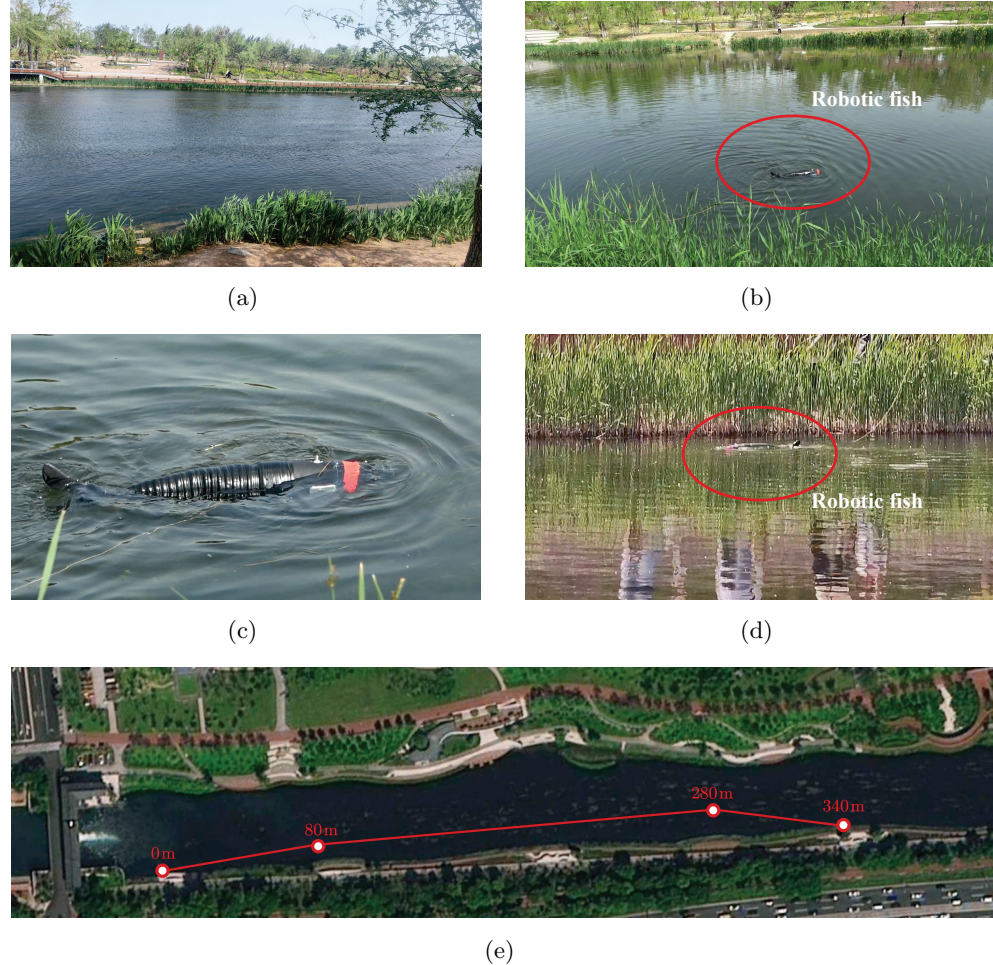


Fig. 15: The on-site experiment images. (a) Field experiment environment. (b) (c) and (d) Photograph captured from the riverbank. (e) Approximate trajectory of robotic fish.

To validate the actual performance of the robotic fish, swimming experiments were conducted in open water. The experimental location is shown in Figure 15a. The robotic fish was continuously tracked and controlled from the shore, as shown

in Figure 15b, 15c, and 15d. To ensure the safety of the robotic fish in case of an emergency and to facilitate its recovery from the water, a safety rope was attached to the fish body. The safety rope does not exert any force on the robotic fish during normal swimming, nor does it affect its motion performance. Figure 15e shows the approximate trajectory of the robotic fish.

In the experimental design, we fully utilized the structural features of the robotic fish. During the initialization phase, in areas with dense aquatic plants along the shore, the robotic fish employed small oscillation amplitudes and high frequencies to counteract the interference from the plants, while enhancing its maneuverability and stability. In contrast, in open water, the robotic fish used large oscillation amplitudes and low frequencies to optimize cruising performance and improve its ability to cope with higher water flow resistance. Meanwhile, using the dynamic model we established, the control parameter was set to 0.3 m/s. The robotic fish swam approximately 340 meters in 12 minutes, with a measured forward speed of around 0.47 m/s. Since the water current was aligned with the swimming direction of the robotic fish, the actual speed was slightly higher than the set control speed.

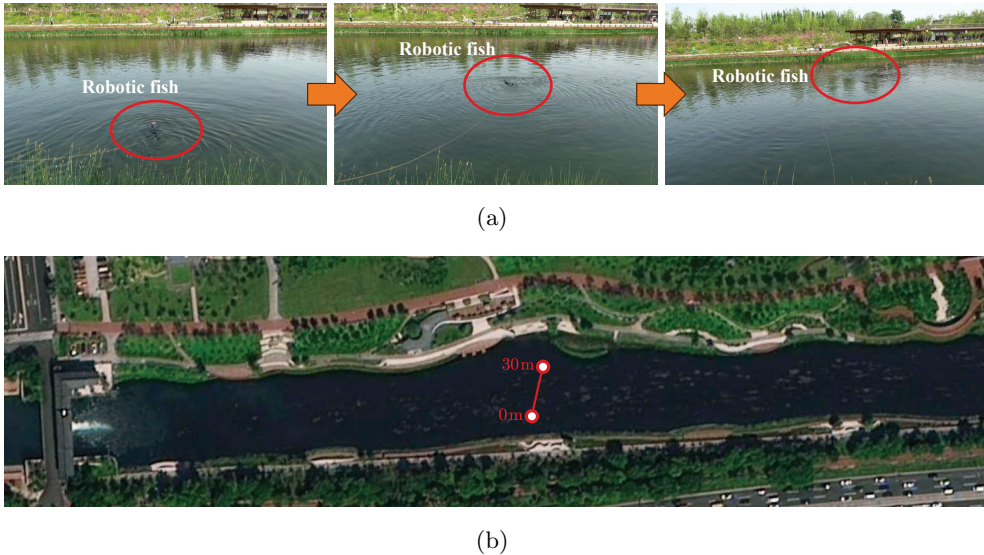


Fig. 16: Image of the cross-river experiment. (a) Photograph of the robotic fish crossing the river. (b) Approximate trajectory of robotic fish.

In addition, to further evaluate the swimming performance of the robotic fish in real aquatic environments, a cross-river experiment was conducted, as shown in Figure 16a. In this experiment, the same control parameter of 0.3 m/s was used, and the robotic fish swam approximately 30 meters in 2 minutes, with the approximate trajectory shown in Figure 16b. During the river crossing, the water flow and wind waves created

resistance against the robotic fish, causing the actual speed to be slightly lower than the set control speed.

6 Conclusion and Future Works

This paper presents a novel wire-driven robotic fish, which is innovative in that it achieves reciprocating tail fin oscillation through continuous motor rotation, with the oscillation amplitude adjusted by switching the rotation direction of the motor. The robotic fish adopts a symmetric dual-transmission submodules structure, effectively avoiding the issues caused by frequent motor reversals. Moreover, the robotic fish is capable of adjusting the amplitude and frequency of tail fin oscillation to adapt to varying environmental conditions. Based on this, a complete kinematic and dynamic model of the robotic fish is developed. Using real experimental data, a data-driven parameter identification method is employed to optimize the hydrodynamic parameters. Further field experiments demonstrate that the robotic fish exhibits excellent swimming stability and environmental adaptability in open water and is capable of completing long-distance autonomous swimming tasks. In the future, we will enhance the autonomy and intelligence of the robotic fish, improve the mechanism to increase swimming speed and flexibility. We will also investigate motion control strategies for diverse field environments.

Declarations

- **Funding** This work was supported by the National Natural Science Foundation of China under Grant 62303020, 62273351.
- **Conflict of interest** The authors declared that they had no known competing financial interests or personal relationships that could have appeared to influence the work.
- **Ethics approval and consent to participate** Not applicable.
- **Consent for publication** All authors have reviewed the manuscript and provided their consent for its publication.
- **Data availability** The datasets generated and analyzed during the current study are available from the corresponding author upon reasonable request.
- **Materials availability** Materials used in this study are available from the corresponding author upon reasonable request.
- **Code availability** The code used in this study is available from the corresponding author upon reasonable request.
- **Author contribution** Runtong Ai: introduction, mechatronic design of the robotic fish, dynamic modeling, experimental validation, writing original draft preparation. Bingxiong Wang, Guohua Yu, Yang Liu, Wenbo Li, Yan Meng: dynamic modeling and experimental validation. Jincun Liu: writing-review and editing.

References

- [1] Yan, S., Wu, Z., Wang, J., Feng, Y., Yu, L., Yu, J., & Tan, M. (2025). Recent advances in design, sensing, and autonomy of biomimetic robotic

- fish: A review. *IEEE/ASME Transactions on Mechatronics*, 30(5), 3517–3536. <https://doi.org/10.1109/TMECH.2024.3469953>
- [2] Zhong, Y., Wang, Q., Yang, J., & Wang, C. (2024). Design, modeling, and experiment of underactuated flexible gliding robotic fish. *IEEE/ASME Transactions on Mechatronics*, 29(3), 2266–2276. <https://doi.org/10.1109/TMECH.2023.3328034>
 - [3] Triantafyllou, M. S., & Triantafyllou, G. S. (1995). An efficient swimming machine. *Scientific American*, 272(3), 64–70.
 - [4] Zhou, X., Xia, K., Tu, H., Zhu, H., Wei, Y., & Qu, F. (2025). Design and hydrodynamic analysis of a dual-drive bionic robotic fish. *Ocean Engineering*, 319, 120234. <https://doi.org/10.1016/j.oceaneng.2024.120234>
 - [5] Wang, M., Zhang, Y., Dong, H., & Yu, J. (2020). Trajectory tracking control of a bionic robotic fish based on iterative learning. *Science China Information Sciences*, 63, 1–9. <https://doi.org/10.1007/s11432-019-2760-5>
 - [6] Wang, J., Wu, Z., Dong, H., Tan, M., & Yu, J. (2022). Development and control of underwater gliding robots: A review. *IEEE/CAA Journal of Automatica Sinica*, 9(9), 1543–1560. <https://doi.org/10.1109/JAS.2022.105671>
 - [7] Liu, J., Zhao, J., Liu, Z., Liu, Y., Ren, Y., An, D., & Wei, Y. (2025). Development and application of the coverage path planning based on a biomimetic robotic fish. *Journal of Field Robotics*, 42(6), 2512–2531. <https://doi.org/10.1002/rob.22531>
 - [8] Wu, Z., Liu, J., Yu, J., & Fang, H. (2017). Development of a novel robotic dolphin and its application to water quality monitoring. *IEEE/ASME Transactions on Mechatronics*, 22(5), 2130–2140. <https://doi.org/10.1109/TMECH.2017.2722009>
 - [9] Wu, Y., Duan, Y., Wei, Y., An, D., & Liu, J. (2022). Application of intelligent and unmanned equipment in aquaculture: A review. *Computers and Electronics in Agriculture*, 199, 107201. <https://doi.org/10.1016/j.compag.2022.107201>
 - [10] Xu, Y., Dong, B., Zheng, C., Zuo, Q., He, K., & Xie, F. (2023). A novel untethered robotic fish with an actively deformable caudal fin. *Advanced Intelligent Systems*, 5(11), 2300276. <https://doi.org/10.1002/aisy.202300276>
 - [11] Berlinger, F., Gauci, M., & Nagpal, R. (2021). Implicit coordination for 3D underwater collective behaviors in a fish-inspired robot swarm. *Science Robotics*, 6(50), eabd8668. <https://doi.org/10.1126/scirobotics.abd8668>
 - [12] Han, J., Fu, Z., Zhang, Y., Shi, L., Kang, R., Dai, J. S., & Song, Z. (2024). Undulatory motion of sailfish-like robot via a new single-degree-of-freedom modularized spatial mechanism. *Mechanism and Machine Theory*, 191, 105502. <https://doi.org/10.1016/j.mechmachtheory.2023.105502>

- [13] Muralidharan, M., & Palani, I. A. (2021). Development of subcarangiform bionic robotic fish propelled by shape memory alloy actuators. *Defence Science Journal*, 71(1). <https://doi.org/10.14429/dsj.71.15777>
- [14] M. R. T. Fokou, Q. R. Xia, H. Jin, M. Xu & E. B. Dong. (2023). A soft robotic fish actuated by artificial muscle modules (SoRoFAAM-1). *Journal of Bionic Engineering*, 20(5), 2030–2043. <https://doi.org/10.1007/s42235-023-00390-6>
- [15] Sfakiotakis, M., Lane, D. M., & Davies, J. B. C. (1999). Review of fish swimming modes for aquatic locomotion. *IEEE Journal of Oceanic Engineering*, 24(2), 237–252. <https://doi.org/10.1109/48.757275>
- [16] Luo, R., Tao, C., & Wang, F. (2025). Design and experimental study of a wire-driven bionic fishtail actuator. *Ocean Engineering*, 317, 120087. <https://doi.org/10.1016/j.oceaneng.2024.120087>
- [17] Liao, X., Zhou, C., Wang, J., & Tan, M. (2024). A wire-driven dual elastic fishtail with energy storing and passive flexibility. *IEEE/ASME Transactions on Mechatronics*, 29(3), 1914–1925. <https://doi.org/10.1109/TMECH.2023.3318219>
- [18] Yang, Q., Wang, Q., Cao, Z., Zhao, Z., Chen, Y., & Zhong, Y. (2025). Development of a wire-driven robotic fish based on double sine mechanism. *Biomimetics (Basel)*, 10(3), 136. <https://doi.org/10.3390/biomimetics10030136>
- [19] Estarki, M., Varnousfaderani, R. H., Ghafarirad, H., & Zareinejad, M. Design and implementation of a soft robotic fish based on carangiform fish swimming. Proceedings of the 9th RSI International Conference on Robotics and Mechatronics (ICRoM), Tehran, Iran, 2021, 322–328.
- [20] Chen, Z., Tian, X., Chen, X., Wen, B., & Li, X. (2023). An experimental study of the wire-driven compliant robotic fish. *Ocean Engineering*, 279, 114433. <https://doi.org/10.1016/j.oceaneng.2023.114433>
- [21] Liang, Y., Wang, K., Mo, Y., & Zhong, Y. A wire-driven flexible vector-propelled robotic fish with omnidirectional adaptive caudal fin. Proceedings of the 29th International Conference on Mechatronics and Machine Vision in Practice (M2VIP), Queenstown, New Zealand, 2023, 1–6.
- [22] Qiu, C., Wu, Z., Wang, J., Tan, M., & Yu, J. (2023). Locomotion optimization of a tendon-driven robotic fish with variable passive tail fin. *IEEE Transactions on Industrial Electronics*, 70(5), 4983–4992. <https://doi.org/10.1109/TIE.2022.3189093>
- [23] Wang, B., Sun, C., Li, D., & Liu, J. (2024). Analysis of a dual tendon-driven robotic dolphin tail: Omnidirectional motions and thrust characteristics. *IEEE Robotics and Automation Letters*, 9(6), 5703–5710. <https://doi.org/10.1109/LRA.2024.3392501>

- [24] Zhong, Y., Li, Z., & Du, R. (2017). A novel robot fish with wire-driven active body and compliant tail. *IEEE/ASME Transactions on Mechatronics*, 22(4), 1633–1643. <https://doi.org/10.1109/TMECH.2017.2712820>
- [25] Liu, J., Zhang, C., Liu, Z., Zhao, R., An, D., Wei, Y., Wu, Z., & Yu, J. (2021). Design and analysis of a novel tendon-driven continuum robotic dolphin. *Bioinspiration & Biomimetics*, 16(6), 065002. <https://doi.org/10.1088/1748-3190/ac2126>
- [26] H. Z. Jiang & Y. W. Liu. (2024). Thrust and drag estimation of a tensegrity robotic tuna by linear acceleration analysis in terms of averaged equation of motion. *Journal of Bionic Engineering*, 21(6), 2804-2816. <https://doi.org/10.1007/s42235-024-00599-z>
- [27] Clapham, R. J., & Hu, H. Isplash-micro: A 50 mm robotic fish generating the maximum velocity of real fish. Proceedings of the IEEE/RSJ International Conference on Intelligent Robots and Systems (IROS), Chicago, USA, 2014, 287–293.
- [28] White, C. H., Lauder, G. V., & Bart-Smith, H. (2021). Tunabot Flex: A tuna-inspired robot with body flexibility improves high-performance swimming. *Bioinspiration & Biomimetics*, 16(2), 026019. <https://doi.org/10.1088/1748-3190/abb86d>
- [29] Yu, J., Zhang, C., & Liu, L. (2016). Design and control of a single-motor-actuated robotic fish capable of fast swimming and maneuverability. *IEEE/ASME Transactions on Mechatronics*, 21(3), 1711–1719. <https://doi.org/10.1109/TMECH.2016.2517931>
- [30] van den Berg, S. C., Scharff, R. B. N., Rusák, Z., & Wu, J. (2022). OpenFish: Biomimetic design of a soft robotic fish for high speed locomotion. *HardwareX*, 12, e00320. <https://doi.org/10.1016/j.hwx.2022.e00320>
- [31] Sfakiotakis, M., Lane, D. M., & Davies, J. B. C. (2002). Review of fish swimming modes for aquatic locomotion. *IEEE Journal of Oceanic Engineering*, 24(2), 237–252. <https://doi.org/10.1109/48.757275>
- [32] Triantafyllou, M. S., Triantafyllou, G. S., & Yue, D. K. P. (2000). Hydrodynamics of fishlike swimming. *Annual Review of Fluid Mechanics*, 32(1), 33–53. <https://doi.org/10.1146/annurev.fluid.32.1.33>
- [33] Triantafyllou, M. S., Triantafyllou, G. S., & Gopalkrishnan, R. (1991). Wake mechanics for thrust generation in oscillating foils. *Physics of Fluids A: Fluid Dynamics*, 3(12), 2835–2837. <https://doi.org/10.1063/1.858173>
- [34] Heo, S., Wiguna, T., Park, H. C., & Goo, N. S. (2007). Effect of an artificial caudal fin on the performance of a biomimetic fish robot propelled by piezoelectric actuators. *Journal of Bionic Engineering*, 4(3), 151–158. [https://doi.org/10.1016/S1672-6529\(07\)60027-4](https://doi.org/10.1016/S1672-6529(07)60027-4)

- [35] Xie, F., Li, Z., Ding, Y., Zhong, Y., & Du, R. (2019). An experimental study on the fish body flapping patterns by using a biomimetic robot fish. *IEEE Robotics and Automation Letters*, 5(1), 64–71. <https://doi.org/10.1109/LRA.2019.2941827>
- [36] Liu, S., Liu, C., Wei, G., Ren, L., & Ren, L. (2025). Design, modeling, and optimization of hydraulically powered double-joint soft robotic fish. *IEEE Transactions on Robotics*, 41, 1211–1223. <https://doi.org/10.1109/TRO.2025.3526087>
- [37] Liao, X., Zhou, C., Zou, Q., Wang, J., & Lu, B. (2022). Dynamic modeling and performance analysis for a wire-driven elastic robotic fish. *IEEE Robotics and Automation Letters*, 7(4), 11174–11181. <https://doi.org/10.1109/LRA.2022.3197911>